JOURNAL OF CATALYSIS **158,** 486–501 (1996)
ARTICLE NO. 0048

Structure and Reactivity of Framework and Extraframework Iron in Fe-Silicalite as Investigated by Spectroscopic and Physicochemical Methods

S. Bordiga,*[,1] R. Buzzoni,* F. Geobaldo,*[,2] C. Lamberti,*[,3] E. Giamello,* A. Zecchina,* G. Leofanti,† G. Petrini,† G. Tozzola,† and G. Vlaic‡

*Dipartimento di Chimica Inorganica, Chimica Fisica e Chimica dei Materiali, Università di Torino, Via P. Guiuria 7, I-10125 Torino, Italy; †ENICHEM Centro di Recerche di Bollate, Via S. Pietro, I-20021 Bollate (Mi), Italy; and ‡Dipartimento di Scienze Chimiche, Via Valerio 38, Trieste and Sincrotone Trieste SCpA, Padriciano 99, I-34012 Trieste, Italy

Received January 13, 1995; revised July 11, 1995; accepted September 26, 1995

The application of IR, Raman, UV–visible, EPR, XANES, EXAFS, and TPR techniques to the determination of the Fe^{3+} local environment in Fe-silicalite is described and discussed. These methods give information concerning the structural changes of the zeolitic structure, upon thermal treatments and interaction with adsorbates. In particular the effect of template burning at 773 K or at 973 K on the local Fe^{3+} environment has been discussed in detail. The reactivity of the zeolite towards NH_3 has also been considered.

INTRODUCTION

Isomorphous substitution of a small fraction (1–2 wt%) of Si^{4+} with Fe^{3+} in silicalite (1) framework leads to the Fe-silicalite structure (2–6). The presence in the zeolitic framework of Fe^{3+} species causes the appearance of an extra negative charge in the framework which must be compensated by cations or by protons in the form of bridged hydroxyls having an acidic strength very close to that observed in H-ZSM-5; in this contribution only the protonic form will be considered. Although the Brønsted acid sites can have similar strength in Fe-silicalite and in H-ZSM-5 (7), it has been reported that the framework stability of the two structures is very different (3): in fact template burning in Fe-silicalite with the associated water production is sufficient to cause the partial rupture of some bonds connecting iron with the oxygens of the framework and to induce migration of the iron into extraframework positions (4, 8, 9). Because of this, a decrease of the framework iron species and the simultaneous appearance of oxidic microaggregates are observed after calcination. Ulan *et al.* have investigated the effect of the gel composition used for the synthesis on the iron distribution in the Fe-silicalite samples obtained (10).

The presence of different iron species has proved to be interesting from the catalytic point of view (11–32): in fact this material, besides the known Brønsted acidic properties (related with the framework iron species) (7) shows very special catalytic activities in oxidation reactions (probably related to extra-framework iron species). The review of Szostak describing the role of postsynthesis treatments on the catalytic properties of zeolites is especially noteworthy (11).

In particular, as shown by Kharitonov *et al.* (12), Fe-silicalite is able to perform one-step oxidation of benzene to phenol by using dinitrogen monoxide as oxidant, with results which are better than those based on processes using supported oxides of vanadium, molybdenum, tungsten, and iron as catalysts. The same group has performed oxidation of benezene to phenol also using nitrous oxide (13), obtaining, with some Fe-ZSM-5 samples, 25% efficiency in benzene conversion with about 100% phenol selectivity. Vorbeck *et al.* (7) report on the conversion of ethylbenzene and *m*-xylene isomerization in Fe-silicalite: the activities for both reactions have been studied in the temperature range 600 K $< T <$ 800 K and compared with those obtained using H-ZSM-5, the protonic form of Fe–Al-silicalites and Fe impregnated silicalites. In that work, also the high activity of Fe-silicalite (compared to that of H-ZSM-5) in the dehydrogenation of ethylbenzene is reported and attributed to the extraframework iron species. Similar studies have also been performed by Kan et al. (14). In the conversion of C_8 aromatics, it has been reported that Fe-silicalite is more selective for xylene production than H-ZSM-5 (15). The *para*-selectivity for the

[1] To whom correspondence should be addressed.

[2] Current address: Dipartimento di Scienza dei Materiali e Ingegneria Chimica, Politecnico di Torino, Corso Duca degli Abruzzi 24, I-10129 Torino, Italy.

[3] Also with INFN Sezione di Torino, Torino, Italy.

0021-9517/96 $12.00

disproportionation of toluene for several metal-substituted silicalites, including Fe-silicalite and B-H-ZSM-5, has also been studied (16).

The role played by iron in N_2O decomposition on Fe-ZSM-5 has been deeply investigated by Panov and coworkers (17–20). Kikuchi *et al.* have observed that, among various metallosilicates, Fe-silicalite was the most active for the reduction of NO by C_3H_6 (21). In a subsequent work (22), they report on the activity of iron-silicalite, having different Si/Fe ratios, in selective reduction of nitric oxide by several hydrocarbons, observing that olefins (C_3H_6 and C_2H_4) were more effective reducing agents than paraffins (C_3H_8 and C_2H_6). They also found that the working temperature for NO reduction by C_3H_6 became lower by decreasing the Si/Fe ratio (i.e. by increasing the extraframework iron species), while NO conversion to N_2 was nearly independent of the iron content; they thus attribute this ability to the framework Si(OH)Fe acid sites. In this field, the recent work of Inui et al. should also be noted (23).

Inui *et al.* (24) had previously reported on the ability of Fe-silicalite to catalyze the conversion of methanol into light olefins. Several groups (25–27) have found that, in methanol conversion, Fe-silicalite has a higher yield and selectivity towards C_2-C_4 olefins than H-ZSM-5. Lin *et al.* (28) have studied the catalytic activity of Fe-ZSM-5, prepared either in basic medium or in neutral fluoride medium, for methanol conversion at 350°C and for toluene methylation reaction at 400°C. They conclude that the acidity induced by the presence of framework Fe cations is of only moderate strength. Nair *et al.* (29) have studied the dehydrogenation of *para*- and *ortho*-ethyltoluene, showing how *para*-ethyltoluene reacts with extraframework Fe species located both in the zeolite pores and at the surface of the micro-particles, while *ortho*-ethyltoluene is able to react only with the surface extraframework iron species. Very recently, Parrillo *et al.* (30) have performed reactivity measurements for *n*-hexane cracking at 427 and 477°C, propene oligomerization at room temperature, and 2-methyl-2-propanol decomposition on H-Fe-ZSM-5, H-Ga-ZSM-5, and H-ZSM-5 and have compared the reactivity of the Brønsted acid sites for the three molecular sieves. A detailed study of the acidity of surface hydroxyls in H-B-ZSM-5, H-Fe-ZSM-5, H-Ga-ZSM-5, and H-ZSM-5 has also been carried out by Chu and Chang (31), who showed the following relation among the acidity strength of the bridged M(OH)Si hydroxyls: SiOH < B(OH)Si ≪ Fe(OH)Si < Ga(OH)Si < Al(OH)Si. Concerning the investigation of hydroxy groups in Fe-silicalites, see also the recent contribution of Datka and Abramowicz (32).

It follows from the above survay that the catalytic properties of Fe-silicalite are strictly related to the characteristics of framework and/or extraframework species, depending upon the reaction to be catalyzed. It therefore becomes a matter of primary importance to understand the changes occurring in the framework upon thermal treatment, starting from a virgin sample still containing the template up to a final sample calcined at high temperature. The location (in framework or extraframework positions) and the oxidation state of the iron species play a role of paramount importance in the determination of acidic, catalytic and shape-selective properties of Fe-silicalite. In this contribution we investigate the structure and the reactivity of both framework or extraframework sites by means of several techniques and we follow the evolution of iron species under the effect of calcination at different temperatures. More specifically we compare the results obtained by the simultaneous application and comparison of IR, Raman, UV–visible, EPR, XANES, and EXAFS spectroscopies and TPR on a pure Fe-silicalite at different treatment stages, in particular Fe-silicalite as synthesized (FeS), calcined in air at 773 K (FeSC1) and finally calcined in air at 973 K (FeSC2). The work gives useful information about the ideal temperature to be used in the calcination process in regard to the desired application of the Fe-silicalite obtained.

In a recent publication, the local environment of Fe^{3+} of sample FeSC1 in vacuo and after NH_3 dosage has been discussed by means of UV–vis and XANES spectroscopies and compared with the local environment of Ti^{4+} in Ti-silicalite (33).

EXPERIMENTAL

Material

To initiate the Fe-silicalite synthesis an alcoholic solution of $FeCl_3$ was added to an alcoholic solution of tetraethyl-ortho-silicate (TEOS). The solution was stirred for 30 minutes, then acidified (pH = 4–5) with H_2SO_4. Tetrapropyl ammonium hydroxide (TPAOH) was then added and the resulting solution was heated to 353 K and held for 5 h before being transferred into an autoclave for hydrothermal synthesis at 440 K for 140 h. The solid was filtered off, washed, with distilled water, and dried at 393 K. X-ray diffraction analysis showed that the zeolite has MFI structure, high crystallinity, orthorhombic symmetry and a unit cell volume of 5369 Å^3. Fe^{3+} insertion into the framework was confirmed by the unit cell volume increase (in comparison with that of pure silicate: 5344 Å^3). Elementary analysis of this material, designated as ''FeS,'' showed that the iron content is Fe = 1.71 wt%.

From the FeS, two different protonic forms, hereafter indicated as FeSC1 and FeSC2, have been obtained by calcining in air at 773 K and at 973 K, respectively.

For TPR experiments a silicalite sample, prepared as described in Ref. (34), has been impregnated with a $Fe(NO_3)_3$ aqueous solution and calcined at 823 K. This compound will be named FeOSil (Fe = 0.91 wt%).

Methods

IR spectra were obtained on a Bruker IFS-66 FTIR spectrometer equipped with a MCT cryodetector. For IR transmission experiments, the samples were in the form of thin self-supporting pellets. For experiments in the IR reflectance mode, intimate dilute mixtures of the zeolite in KBr were used. The Raman spectra were obtained on a Perkin Elmer 2000R NIR-FT Raman spectrometer equipped with a InGaAs detector. The lasing medium was a Nd-YAG crystal pumped by a high pressure krypton lamp and the wavelength used was 1064 nm. The power output was approximately 1000 mW. The UV–vis reflectance spectra were carried out on a Varian Cary 5 spectrometer, on a powdered Fe-silicalite sample. The TPR experiments were carried out in a typical gas chromatographic apparatus (H_2 5% in Ar, heating rate 10 K min^{-1}). EPR spectra have been obtained on a Varian E 109 spectrometer equipped with dual cavity and operating in the X band. Varian Pitch was used as a reference for calibration of g values.

XANES and EXAFS spectra have been obtained at the EXAFS3 beam line of LURE in Orsay, France. The storage ring was operated at 1.85 GeV, a typical beam current being of 300 mA. The X-ray source was monochromatized by using a double crystal Si(311) monochromator detuned to eliminate harmonics. The step size was 0.3 eV for near edge spectra and 2.0 eV for the extended spectra. Measurements were performed in the transmission mode, by using air filled ionisation chambers. Energies were calibrated by means of a Fe foil internal standard (Fe edge 7112 eV). XANES spectra were background subtracted with a linear function in the energy range 7090–7110 eV; the spectra were then normalized to unity in the continuum at 7190 eV. EXAFS spectra were analyzed following standard procedures using Michalovicz programs (35). A polynomial function (third degree) has been used to extract the EXAFS spectrum. The Fourier Transform of the EXAFS spectrum has been obtained multiplying by k^3 in the range 4–13 $Å^{-1}$ using a Kaiser window ($\tau = 3$). Quantitative data have been obtained by fitting the Fourier-filtered signal of the first peak with a theoretical signal, using a nonlinear least-squares routine (36). All the EXAFS data here reported have been obtained extracting the experimental phase shift and amplitude functions from a model compound ($FePO_4$). The data analysis on the same experimental data has also been achieved using the theoretical curves derived from McKale *et al.* (37), and the obtained results are consistent, within the experimental errors, with that obtained using the experimental phase shift and amplitude functions.

Suitably designed quartz cells with two different compartments (allowing *in situ* outgassing under vacuum, $p = 10^{-2}$ Pascal, and gas or liquid dosages via the gas phase) have been adopted in order to allow a careful control of Fe-silicalite structural changes, induced by thermal treatments or interaction with adsorbates.

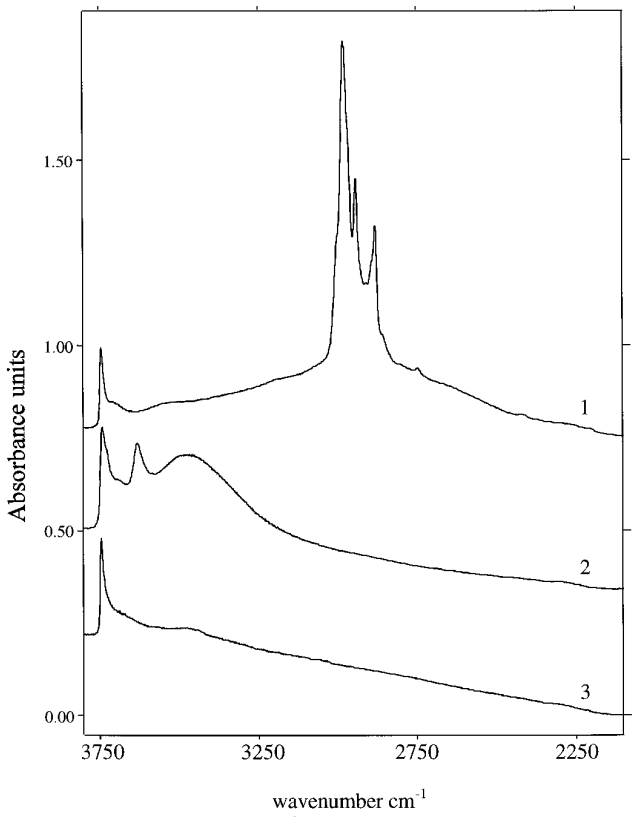

FIG. 1. IR spectra of Fe-silicalites in the OH stretching region: (1) FeS outgassed at 500 K; (2) FeSC1 outgassed at 673 K; (3) FeSC2 outgassed at 673 K.

RESULTS AND DISCUSSION

1. IR and Raman Spectra

Infrared spectroscopy is a convenient tool to characterize the structural properties of molecular sieves and has been extensively utilized in the study of pentasil zeolites (38–40). Meaningful information concerning the iron structure in the zeolitic framework has been obtained by exploring both the hydroxyl stretching (3800–3400 cm^{-1}) and framework (1350–400 cm^{-1}) regions (40).

The effect of calcination in air at 773 K and 973 K on the IR spectrum of a Fe-silicalite is illustrated in Fig. 1 where the spectra of FeS, FeSC1 and FeSC2 are compared (3800–2000 cm^{-1}).

To assign the spectra let us first briefly recall that the whole wavenumber range (4000–600 cm^{-1}) of the zeolite mid-IR spectrum can be divied into three intervals: (i) $\nu < 1250\,cm^{-1}$, the region characteristic of the fundamental

framework modes (discussed in the next paragraph); (ii) $2000 < \nu < 1500$ cm^{-1}, the region of the overtones and combination framework modes; (iii) $3800 < \nu < 2000$ cm^{-1}, the region of vibrational modes of the hydroxyl groups (38). In particular, free silanols absorb at 3750–3700 cm^{-1}; Brønsted acid sites absorb at 3670–3610 cm^{-1} and hydrogen-bonded silanols at 3500–3250 cm^{-1}. Of course in the spectrum of FeS the bands of the template must be considered as well.

(*a*) *Evolution of the OH stretching bands.* By outgassing the FeS sample at 500 K, spectrum 1 of Fig. 1 is obtained, whose main spectroscopic features can be summarized as follows:

(i) an intense peak centred at 3745 cm^{-1} (with an evident shoulder at lower frequency) which is readily assigned to isolated (free) silanol groups mainly present on the external surfaces of the zeolitic microparticles;

(ii) a broad absorption extending from 3600 to 2500 cm^{-1} (on which the narrow CH_2 and CH_3 template stretching modes at 3100–2850 cm^{-1} are clearly superimposed) assigned to the OH stretching of the template (because TPAOH has been used in the synthesis). The lowered frequency and the large half-width, reveals that the hydroxyl groups are strongly interacting through hydrogen bonding (41).

The template removal (obtained by calcination in air at 773 K), followed by activation in vacuo at 673 K, induces strong changes in the IR spectrum (especially in the 3800–2000 cm^{-1} range) as documented by spectrum 2 of Fig. 1. In fact the bands characteristic of the template disappear while a peak at 3630 cm^{-1} due to bridged hydroxyls with Brønsted acid character grows in a parallel way. The structure of these sites is shown in Scheme 1.

The corresponding band in the analogous Al containing structure (H-ZSM-5) is observed at 3610 cm^{-1} (39); the higher frequency value found for the Fe-silicalite indicates a lower acid strength of the Brønsted sites associated with Fe^{3+}. This is in agreement with the observation that iron-containing ZSM-5 is able to perform selective dehydroxylation reactions, while with ZSM-5 complete cracking occurs (14). We discuss elsewhere about lower acidity of these species by studying their interaction with CO and N_2 at 77 K (42); see also the contribution of Kustov *et al.* in Ref. (43).

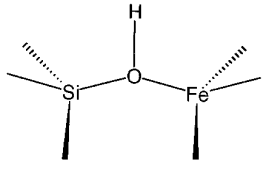

SCHEME 1

The comparable intensity of the peak at 3630 cm^{-1} (Fe-silicalite) and at 3610 cm^{-1} (H-ZSM-5 with similar Fe and Al content) indicates unequivocally that after calcination at 773 K a high concentration of Fe^{3+} is still present into the zeolitic framework.

Nevertheless, the formation of a broad absorption centred at 3450 cm^{-1} due to hydrogen-bonded silanolic species suggests that the template removal by thermal activation is accompanied by some extraction of Fe^{3+} with formation of hydroxyl nests. In fact similar manifestations have been found only in defective silicalite and in dealuminated H-ZSM-5, and have consequently been attributed to formation of fully hydroxylated nanovoids (nests) (38).

Calcination in air at 973 K (spectrum 3) followed by activation in vacuo at 673 K causes a dramatic erosion of the peak associated with the Brønsted acid sites (3630 cm^{-1}). This can be interpreted on the basis of massive Fe^{3+} migration from framework towards extraframework positions. The very small residual intensity of the absorption centred at 3630 cm^{-1} (Brønsted sites) after this treatment indicates that the amount of Fe^{3+} anchored to the zeolitic frame is small and that the majority of Fe^{3+} is now in extra-framework positions, possibly in the form of oxidic microaggregates. Beside the disappearance of the 3630 cm^{-1} peak, we also notice the elimination of the broad absorption centred at 3450 cm^{-1}, associated with hydroxylated nests.

This can be explained by considering that the high temperature reached during the calcination of the FeSC2 sample has induced a deep rearrangement of the zeolitic structure (38, 39), with diminution of the defect concentration.

(*b*) *Evolution of framework stretching bands.* Framework stretching modes with prevailing Si–O character are expected in the 1300–700 cm^{-1} interval. These modes may derive from the stretching vibrations of the [SiO_4] tetrahedral primary building unit split by crystal field effects (40). In particular the absorption in the 1300–1000 cm^{-1} range can be interpreted as deriving from the asymmetric modes with T_2 (IR active) symmetry in the isolated [SiO_4] units, while the absorption in 800–700 cm^{-1} interval derives from the symmetric mode with A_1 (Raman active) symmetry in the isolated [SiO_4] tetrahedron. Another equivalent explanation is in terms of the asymmetric and symmetric modes of the simpler SiOSi unit (3, 6). Both explanations are sufficient to justify the presence of two main absorption bands in the IR and Raman spectra together with their relative intensities. It has been shown that in some cases the presence in the framework of nests covered by silanols or of a small concentration of heteroatoms is sufficient to induce well defined spectral modifications in the framework stretching region. A more complete discussion of the problem is given in Ref. (40), where the effects of hydroxyl

groups and of the isomorphous substitution in silicalite of Ti, Fe, and B on the IR and Raman spectra are considered and discussed in detail.

Coming now to the iron-substituted silicalites, new absorption in both IR and Raman spectra are observed (see Fig. 2): in particular, a shoulder at 1006 cm^{-1} (indicated by an arrow) partially overshadowed by the strong absorption centred at 1150 cm^{-1} (curve 1) and a peak at 1025 cm^{-1} (curve 1 in the inset) are detected in the IR and Raman spectra, respectively.

The modification of the IR spectrum is quite modest: this is due to the proximity of the Fe-sensitive mode at 1006 cm^{-1} to the stronger fundamental mode of the unperturbed framework (which thus overshadows the Fe-sensitive band) and to the broad absorption in the 950–900 cm^{-1} interval (associated with Si-OH groups) which is also interfering with the Fe-sensitive mode. This latter band is typical of silicalites containing a high concentration of silanols located in internal nests (40).

The bands at 1006 cm^{-1} can be explained on the basis of a fully ionic model: in this case the local structure surrounding the framework Fe^{3+} species is described by 4 $[O_3Si\text{-}O]^-$ units, as shown in Scheme 2.

On this highly simplified basis (in reality the structure is only partially ionic) the novel features observed in the IR spectra can be considered to a first approximation as

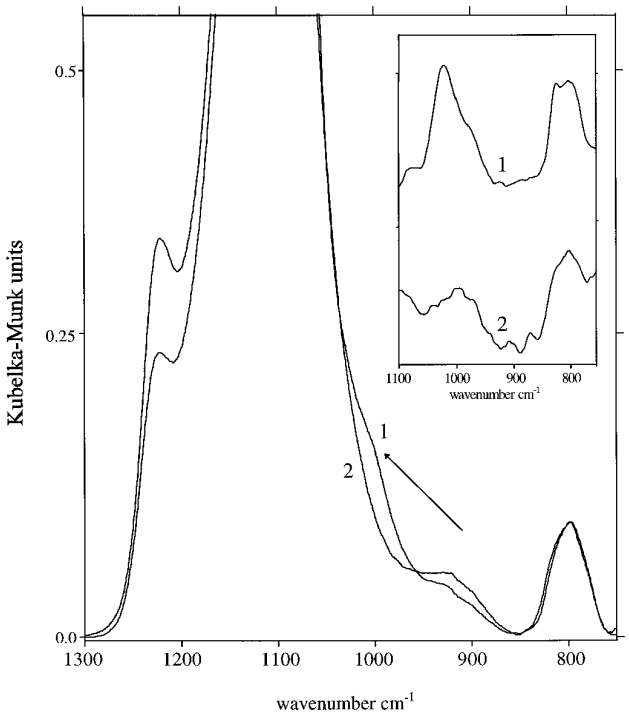

FIG. 2. Framework stretching modes of Fe-silicalites. Diffuse reflectance IR spectra of diluted mixture of zeolites with KBr: (1) FeSC1; (2) FeSC2; In the inset Raman spectra: (1) FeSC1; (2) FeSC2.

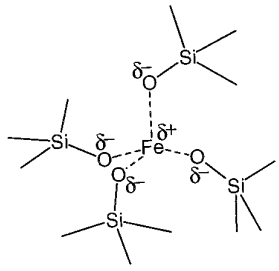

SCHEME 2

highly localized vibrational modes of the tetrahedra surrounding the Fe^{3+} centre. Due to the proximity of the bands characteristic of Fe-silicalite to those of the unpertubed skeletal modes, it can be hypothesized that the new bands at 1006 cm^{-1} (IR) and 1025 cm^{-1} (Raman), are mainly associated with the vibrational modes of the O_3SiO^- units surrounding the Fe^{3+} centre. Indeed, as $[O_3Si\text{–}O]^-$ units have approximate C_{3v} symmetry, a local mode with A_1 character (mainly a $Si\text{–}O^-$ stretching) is expected to emerge from the complex absorption in the 1250–1000 cm^{-1} range (where the skeletal modes with T_d character are actually absorbing). This is the reason why in Raman spectra, where only A_1 modes are intense, this fingerprint band is strong and evident (spectrum 1 in the inset of Figure 2). A similar explanation has been advanced for the fingerprint band of Ti-silicalite (40). In this case, however, the band has a more pronounced Ti-O stretching character: this is due to the fact that the intrinsic modes of $[TiO_4]$ and $[SiO_4]$ units in tetrahedral compounds have similar frequencies. On the contrary, the intrinsic frequency of IR (857 cm^{-1}) and Raman (762 cm^{-1}) (44, 45) modes of $[FeO_4]$ units in tetrahedral compounds is distinctly lower than that of the analogous $[SiO_4]$ groups: hence the admixture of Si–O and Fe–O stretching in the fingerprint band is lower than in the previous case.

Calcination treatment at 973 K causes the disappearance of the IR shoulder at 1006 cm^{-1} and the erosion of the Raman band at 1025 cm^{-1} (curves 2 of Fig. 2): this clearly indicates that a decrease of the concentration of the framework Fe^{3+} species is occurring. It is concluded that thermal treatments at high temperature and in presence of water vapor favor the breaking of the bonds connecting iron with the framework and its migration into extraframework sites.

2. UV–Visible Spectra

Electronic spectroscopy in the UV–visible region is a useful technique for studying the electronic state of isolated transition metal ions (46). In this contribution UV–vis spectroscopy is applied to study the structural modifications involving Fe^{3+} species induced by: (i) calcinations in the 773–973 K interval, (ii) vacuum treatments at 673 K, and (iii) interactions with adsorbates.

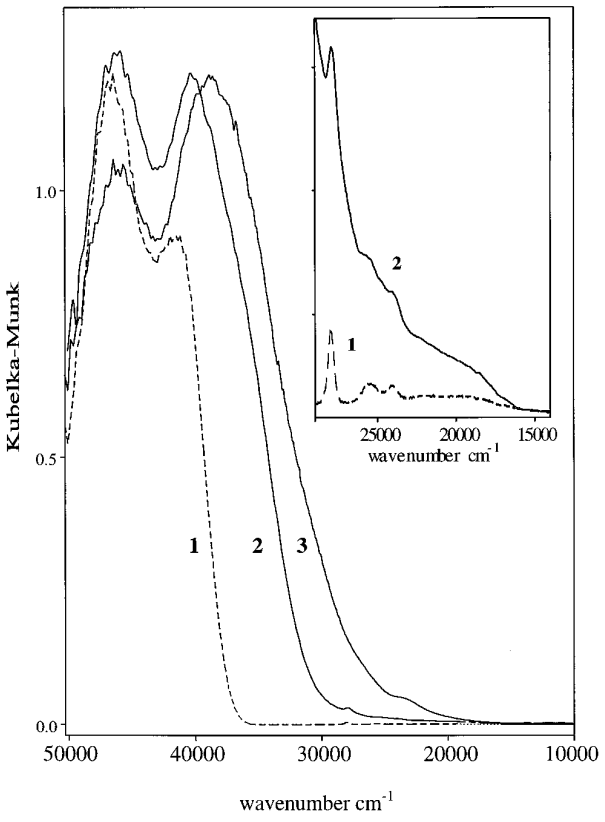

FIG. 3. UV–visible reflectance spectra of Fe-silicalite samples equilibrated to the ambient atmosphere: (1) FeS (broken line); (2) FeSC1; (3) FeSC2. In the inset an exploded view of the *d–d* transitions: (1) FeS; (2) FeSC1.

The UV-visible reflectance spectra of FeS, FeSC1 and FeSC2 samples (obtained in presence of the ambient atmosphere) are reported in Fig. 3.

Two common (and very relevant) features can be observed in all spectra since they are dominated by: (i) a strong absorption in the 50,000–30,000 cm^{-1} interval (two maxima are clearly distinguished) with ligand to metal Fe^{3+} charge transfer character involving isolated framework Fe^{3+} (28, 47, 48), and (ii) weak peaks in the 30,000–17,000 cm^{-1} range, related with *d–d* transitions (6, 28, 47–49).

In the inset (a) an exploded view (×10) of the interval corresponding to the *d–d* transitions is reported to show the structure of the spectrum. In the following discussion, the transitions with charge transfer character (CT) will be considered separately from the *d–d* ones, because their interpretation can be more conveniently made following two different approaches, one involving molecular obital theory (CT bands) and the other crystal field theory (*d–d* bands).

(*a*) *d–d bands.* The *d–d* spectrum of Fe-silicalite (FeS), is characterized by five bands at 19,000 (broad), 22,000 (broad), 24,000, 25,530, and 28,000 cm^{-1}. These absorptions are assigned by considering the Fe^{3+} ion (d^5 configuration) in tetrahedral symmetry (see Scheme 3, where the splitting of the free ion terms (^6S, ^4G, ^4D) induced by a weak crystal field is illustrated). From Scheme 3 it can be inferred that, as the ground state of Fe^{3+} ion is $^6A_1$, the five extremely weak observed bands correspond to the forbidden transitions $^6A_1 \rightarrow {}^4T_1$; $^6A_1 \rightarrow {}^4T_2$, $^6A_1 \rightarrow {}^4E$, $^4A_1$ (at the same energy as ^4E), $^6A_1 \rightarrow {}^4T_2$ and $^6A_1 \rightarrow {}^4E$ (see arrows in the Scheme 3). The energy scale reported in this scheme is qualitative.

More quantitative information can be obtained by using the Tanabe and Sugano diagram for a d^5 configuration in tetrahedral symmetry (6), which allows estimation of the energy scale for the configurations and the value of 10Dq (about 7000 cm^{-1}). Also the sharp character of the band at 28,000 cm^{-1}, corresponding to the $^6A_1 \rightarrow {}^4E$ transition, is easily explained on the basis of the Tanabe–Sugano diagram. In fact the energy of the final ^4E (derived from the ^4D term) state appears to be nearly independent of the magnitude of Dq (directly correlated with the Fe^{3+} symmetry); small distortions from this ideal symmetry induced by vibronic coupling (normally the main source of broadening) will not have an influence on this transition. Analogous considerations can explain the sharp character of the $^6A_1 \rightarrow {}^4T_2$ and of the $^6A_1 \rightarrow {}^4E$, $^4A_1$ transitions and of the broader shape of the two *d–d* bands at lower frequency.

The agreement of the experimental data with crystal field theory together with their accordance with the spectroscopic manifestations derived from literature data of model compounds (where Fe^{3+} is in tetrahedral coordination) such as $FePO_4$, Fe^{3+} in $AlPO_4$ and other analogous compounds, suggests that in FeS the Fe^{3+} ions are in tetrahedral lattice positions. Owing to the similarity of the Tanabe and Sugano diagram of tetrahedral and octahedral complexes, this conclusion cannot be considered as unequivocal and only the comparison with the results deriving from others spectroscopies will allow the final assignment to be made (*vide infra*).

(*b*) *CT bands.* A molecular orbital scheme for a tetrahedral complex of Fe^{3+} with σ-π character is used as starting point for a discussion of the transitions with ligand to metal charge transfer character absorbing in the 50,000–30,000 cm^{-1} range. The complete molecular orbital dia-

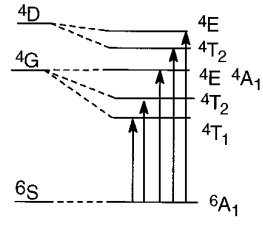

SCHEME 3

gram of a complex with both σ and π contributions is reported elsewhere (50). For this discussion, it is sufficient to know that the highest occupied molecular orbital (with pure ligand character) has t_1 symmetry, while the orbitals with higher energy have e and t_2 symmetry. These orbitals with prevailing metal character are only partially filled. For a d^5 system (Fe^{3+}), the $e^2t_2^3$ configuration is favoured with respect to $e^4t_2^1$, because high spin configurations are always favoured in tetrahedral coordination (the crystal field is not strong enough to cause spin-pairing) (46). On this basis the two bands observed at 46,500, and 41,500 cm^{-1} (curve 1 in Fig. 3) can be assigned to the $t_1 \rightarrow t_2$ and $t_1 \rightarrow e$ transitions involving Fe^{3+} in the [FeO_4] tetrahedral group.

As mentioned for the d–d transitions, octahedral complexes of Fe^{3+} are also characterized by two strong bands in the same energy range (48, 50), so the presence of two bands in the 50,000–30,000 cm^{-1} region considered alone cannot be taken as a conclusive proof of the tetrahedral coordination state of Fe^{3+}.

(*c*) *Effect of calcination.* The template removal obtained by calcination at 773 K (FeSC1) induces clear modifications in the UV–visible spectrum, especially in the range where the transitions with charge transfer character occur (curve 2 of Fig. 3).

In particular we observe: (i) a broadening of the CT peak at 46,500 cm^{-1}; (ii) a parallel shift towards lower wavenumber of the second CT maximum (now centred at 40,250 cm^{-1}; (iii) an evident absorbance increase in the low wavenumber tail of the lowest CT band (36,000 cm^{-1}) which is extended down to the d–d region; (iv) a broadening of all the d–d bands. All these results suggest that calcination induces a decrease of the concentration of tetrahedral framework Fe^{3+}, with formation of Fe^{3+} species with different coordination state. However, quantification of this transformation cannot be made on the sole basis of the UV–visible spectra. The hypothesis of a structural transformation induced by the thermal treatment is confirmed by the difference spectrum, (FeSC1–FeS) (Fig. 4a) where the formation of the strong asymmetric peak with a maximum at 36,000 cm^{-1} and the simultaneous disappearance of a band centred at 46,000 cm^{-1} (negative band) are clearly observed.

To infer the coordinative state of these new Fe^{3+} species it is very useful to review some literature data, and in particular those concerning isolated Fe^{3+} species in octahedral complexes and in small clusters obtained by hydrolysis of Fe^{3+} complexes. Thus, (i) Fe^{3+} species in octahedral complexes are always characterized by a strong CT absorption at about 36,000 cm^{-1} (as in the case of the Fe^{3+} in Al_2O_3 (48)); (ii) octahedral Fe^{3+} present in small clusters shows strong and broad absorptions at about 30,000 cm^{-1} as observed for clustered Fe^{3+} in hydroxides (51). The agreement of these data with the main manifestation obtained in the difference spectrum (i.e., formation of a strong and asymmetric band with maximum at 36,500 cm^{-1} upon heating at 773 K), suggests that calcination induces partial Fe^{3+} migration from framework toward extraframework positions with formation of isolated and/or clustered species.

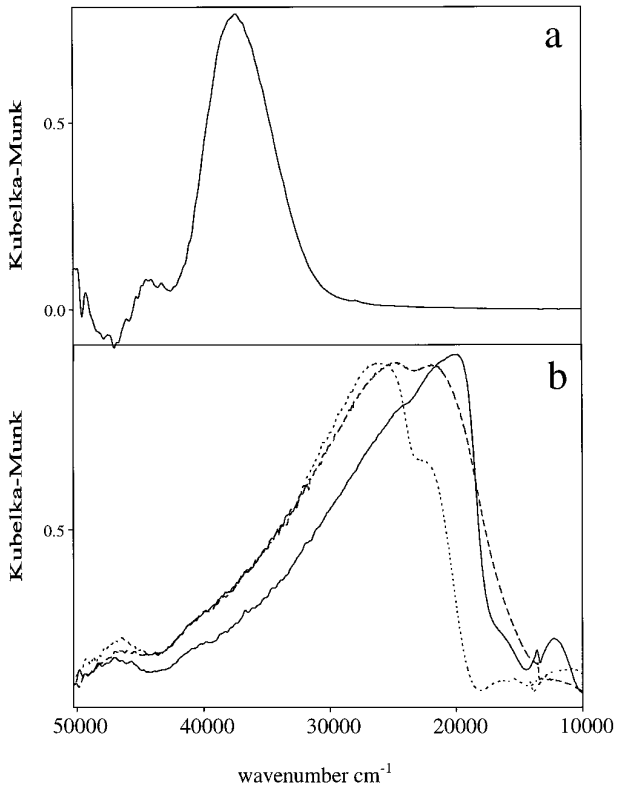

FIG. 4. UV–visible reflectance spectra: (a) difference spectra between curves 2 and 1 of Fig. 3. (b) full line, Fe_2O_3 diluted in SiO_2; dotted line, γ-FeOOH diluted in SiO_2; broken line, $Fe(OH)_3$ diluted in SiO_2.

Although the analysis of the d–d region of the FeSC1 spectrum (curve 2 in Fig. 3) is not easy because the d–d transitions are partially overshadowed by the tail of the CT bands, nevertheless, from a qualitative point of view it can be inferred that calcination induces only a broadening of the d–d transitions, without alteration of the basic 5-band pattern. This result is not in contrast with the previously advanced hypothesis. In fact for a d^5 configuration, the term diagrams for tetrahedral and octahedral symmetry are identical (46). For these reasons the substantial invariant character of the d–d bands before and after the thermal treatment is not in contrast with the hypothesis of (at least a partial) Fe^{3+} migration from framework tetrahedral coordination state to extraframework positions with higher coordination state. In conclusion, the broadening of the d–d bands can be simply justified by the simultaneous presence of different Fe^{3+} coordination states (tetrahedral and octahedral) and slightly different 10 Dq.

The effect of calcination at 973 K on a Fe-silicalite sample (shown in Fig. 3, spectrum 3) adds further evidence to the previous picture. In fact, (i) in the charge transfer region there is a clear intensity decrease of the peak centred at 46,000 cm^{-1}; (ii) a second absorption at 38,700 cm^{-1} becomes the most evident feature of the spectrum (the low frequency tail of this CT component definitely overshadows the *d–d* transitions, which thus cannot be observed at all). It is evident that while the residual band at 46,000 cm^{-1} is ascribable to isolated Fe^{3+} species (tetrahedral and/or octahedral), that at 38,700 must be assigned to clustered Fe^{3+}. In our opinion the shift of the absorbing edge towards the lower wavenumber induced by the most severe thermal treatments suggests that clusters of increasing size are contributing heavily. The appearance of a broad absorption centred at 23,400 cm^{-1} on FeSC2 adds further evidence. In fact, while on the one hand it cannot be ascribed to a new *d–d* transition (because the intensity is higher by about an order of magnitude), on the other hand it is also found in the UV–vis spectra of ferric oxides diluted with silica (these spectra are reported in Fig. 4b): we thus think that it must be ascribed to Fe^{3+} species present in the form of massive oxidic microaggregates (Fe_2O_3 particles). A quantitative estimation of their concentration is however not possible by reflectance spectroscopy. In conclusion, the thermal treatment at 973 K causes massive migration of Fe^{3+} into extraframework positions with formation of clustered Fe^{3+} species (probably trapped in the channels or at their intersections) and Fe_2O_3 particles.

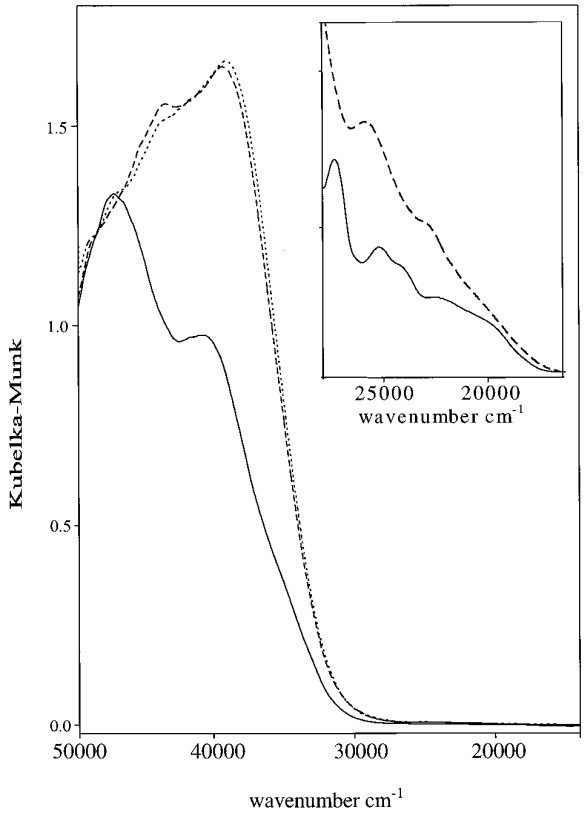

FIG. 5. UV–visible reflectance spectra of FeSC1: the effect of vacuum treatment and NH_3 adsorption: broken line, outgassed at 673 K, full line, after 60 Torr of NH_3; dotted line, outgassed at 673 K.

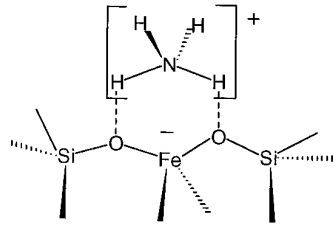

SCHEME 4

(*d*) *Effect of outgassing and adsorbates dosage.* The effect of vacuum treatment of the FeSC1 sample and its interaction with adsorbates is illustrated in Fig. 5. A vacuum treatment at 673 K (broken line) induces substantial changes in the CT and *d–d* regions (the *d–d* interval is also reported in the inset with larger magnification). In particular in the CT region, a strong and broad absorption extending from 50,000 to 32,000 cm^{-1} with a maximum at 38,000 cm^{-1} is formed while in the *d–d* region the individual bands of the *d–d* multiplet are broadened. Dosage of gaseous NH_3 causes an abrupt change of the CT and *d–d* spectra (full line in Fig. 5) with the restoration of a spectrum (characterized by distinct adsorptions similar to those observed in case of the "as synthesized" sample (except for the broad absorption at low frequency). In case of H_2O dosage we observe analogous effects, but the spectrum change is less spectacular. The phenomenon is reversible, as shown by the dotted line reported in Fig. 5 (obtained after evacuation at 673 K). This behavior is clearly indicative that the previously discussed modifications are associated with changes of the coordination state of Fe^{3+} species induced by removal or insertion of ligands. The broad nature of the absorptions of samples activated *in vacuo* (when compared with those obtained after NH_3 or H_2O contact) indicate unequivocally that vacuum treatments cause the formation of Fe^{3+} species with a reduced symmetry. A plausible interpretation is as follows.

(a) In the presence of NH_3 the framework Fe^{3+} species are in a perfect tetrahedral symmetry, as the charge balancing can be made by NH_4^+ (Scheme 4). In the case of H_2O the formation of H_3O^+ is uncertain (52–53); however, the formation of a strong H-bond interaction can have similar effects. Vacuum treatments, by inducing the desorption of ligands, give bridging hydroxyl groups anchored to the oxygens by more covalent bonds. This is accompanied by a distortion in the $[FeO_4]^-$ units as shown in Scheme 5

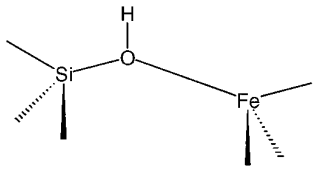

SCHEME 5

with loss of the perfect T_d symmetry. The degenerate levels characteristic of the perfect tetrahedral structure are consequently expected to split into multiplets. The expected effect will be a distinct broadening as observed.

(b) Analogous conclusions can be inferred for isolated extraframework Fe^{3+} species. In fact these ions should show octahedral symmetry in the presence of H_2O and NH_3 (being completely solvated in the zeolite cavities) and assume lower symmetries *in vacuo* (where they have moved towards the zeolite walls to increase the oxygen ligancy).

(c) Finally, in the case of clustered species containing a high percentage of surface Fe^{3+} ions (with local symmetry lower than T_d or O_h) the adsorption of NH_3 or H_2O ligands brings the surface ions towards a more symmetrical (sixfold coordinated) situation.

The effect of vacuum treatment at 673 K is very modest in the case of the samples calcined at 973 K (FeSC2). In fact the UV–visible spectra obtained *in vacuo* and in ambient atmosphere are not sensibly different and even direct H_2O or NH_3 adsorption does not induce significant modifications. This behaviour can be explained if the spectrum, in the *d–d* region characteristic of isolated Fe^{3+} ions, is dominated by the CT manifestations of large oxidic microaggregates, shifted toward the frequency characteristic of Fe_2O_3 (Fig. 4b). It is the presence of this strong band which does not allow the observation of any spectral changes (in the *d–d* region) associated with coordination changes at the exposed Fe^{3+} centers.

In conclusion, UV–visible spectroscopy reveals substantial differences between FeSC1 and FeSC2 samples as far as the Fe^{3+} coordination state is concerned. In particular, the FeSC1 sample contains mainly framework Fe^{3+} and (to a smaller extent) isolated or small clustered extraframework species. The coordinative state and the local symmetries of these species are strongly affected by the presence or absence of extra ligands such as H_2O and NH_3. On the contrary, the FeSC2 sample appears to be mostly constituted by extraframework Fe^{3+} species in the form of clusters and large oxidic microaggregates which are, apparently, little affected by adsorbates.

3. TPR

Further data which confirm this picture are obtained from the analysis of the temperature programmed reduction (TPR) curves. TPR experiments show peaks in correspondence with the reduction temperature characteristics of the reducible species (54). The area of the peaks is proportional to the amount of H_2 consumed in the reduction reaction transforming Fe^{3+} into Fe^0. The results concerning FeSC1, FeSC2, and FeOSil samples are reported in Fig. 6.

The TPR curves of FeSC2 and of FeOSil samples (full line and broken line, respectively) are characterized by single maxima in the 650–700 K interval. The ratio between the peak area of FeOSil and FeSC2 (0.50) is in good agreement with the ratio obtained by elementary analysis (0.53). The similarity of the reduction pattern of FeSC2 and FeOSil (where the iron is certainly in the form of Fe_2O_3 microparticles) implies that similar species are also present in FeSC2. This implies that after high temperature calcination, the iron is completely in extraframework positions.

The TPR curve of FeSC1 (dotted line in Fig. 6) shows two maxima centered at 693 K and 993 K. The peaks are sufficiently separated to allow the identification of two distinct families of Fe^{3+} species. The first reduction peak is in the same temperature interval as found for FeSC2 and so it is easily ascribed to extraframework Fe^{3+} species. The ratio between the area of this peak and that of FeSC2 is ~0.20–0.25. This indicates that FeSC1 is characterized

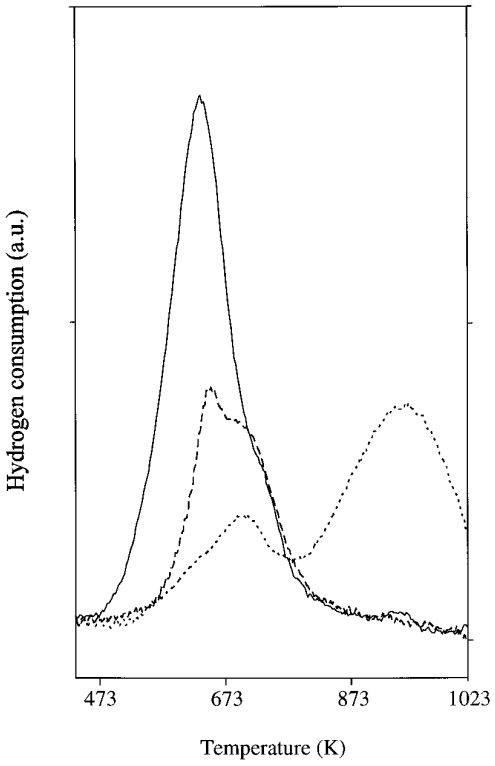

FIG. 6. TPR: full line, FeSC2; broken line, FeOSil; dotted line, FeSC1.

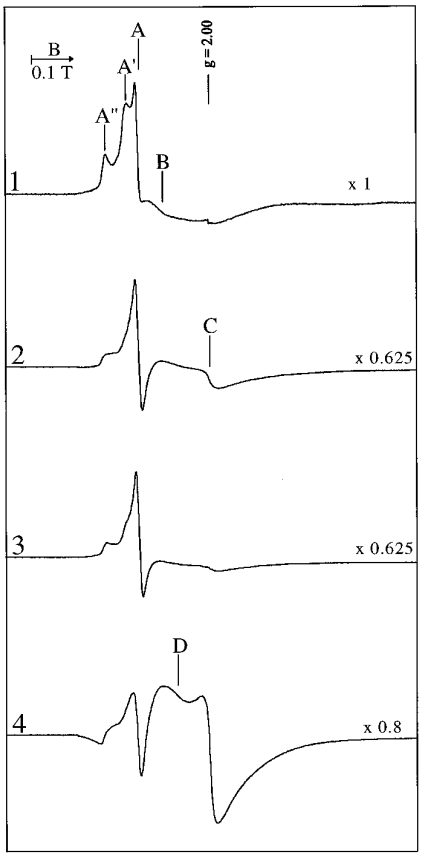

FIG. 7. EPR spectra of FeSC1 recorded at 77 K: (1) after evacuation at 673 K; (2) after H_2O adsorption at room temperature; (3) after outgassing at room temperature; (4) after NH_3 adsorption (60 Torr) at room temperature.

by ~20–25% of extraframework species. The second peak, observed at very high temperature (993 K), is ascribed to a residual fraction (~0.80–0.75%) of framework Fe^{3+} species of difficult reducibility. The relevant temperature difference observed for the two peaks is indicative of the great shielding effect of the zeolitic framework, which protects the framework Fe^{3+} from hydrogen attack.

4. EPR

The ferric ions observed in various zeolitic systems (including the present one) are usually in high spin $3d^5$ configuration ($S = 5/2$, ^6S as ground state of the free ion): this implies, in EPR spectroscopy, that the main spectral features are actually determined by the zero field splitting (ZFS) parameters D and E which, in their turn, depend on the strength and symmetry of the crystal field.

The spin-Hamiltonian operator H is, at the second-order approximation

$$\hat{H} = \mu_B \mathbf{B} \cdot \mathbf{g} \cdot \mathbf{S} + D\{S_z^2 - 1/3(S(S+1))\} + E(S_x^2 - S_y^2)$$

where μ_B is the Bohr magneton, and **B** the external magnetic field vector, **S** is the spin vector, of components S_x, S_y, and S_z, and $S = 5/2$ is the spin of the Fe^{3+} ions. Making the usual approximation for Fe^{3+}, it can be assumed that E and D are small, and **g** becomes isotropic. The various lines in the EPR spectra are usually discussed in terms of g_{eff}, where $g_{eff} = h\nu/\mu_B \mathbf{B} \cdot \mathbf{S}$.

The EPR spectra of FeSC1 recorded at 77 K and 300 K, after outgassing the sample at 673 K, are reported in Figs. 7 and 8 (spectra 1), respectively.

The two spectra are determined by the overlapping of various spectral lines. At low temperature (Fig. 7, spectrum 1) a line at $g_{eff} = 4.3$ (signal A) dominates the spectrum but, differently from what is observed in the case of other similar samples (28), lines at $g_{eff} \cong 5.5$ (A') and $g_{eff} \cong 8.9$ (A'') are also present and appear as shoulders of the main signal. At higher fields a very broad line (B) is observed centered between $g_{eff} = 2.5$ and $g_{eff} = 3.0$, and no signal is observed at $g = 2.0$. The spectral profile undergoes a severe change if the spectrum is recorded at 298 K (Fig. 8, spectrum 1) due to the dramatic increase of the intensity of the line B which, therefore, does not follow the Curie law. This behavior of line B with increasing temperature (accompanied by g shift and linewidth modification) indi-

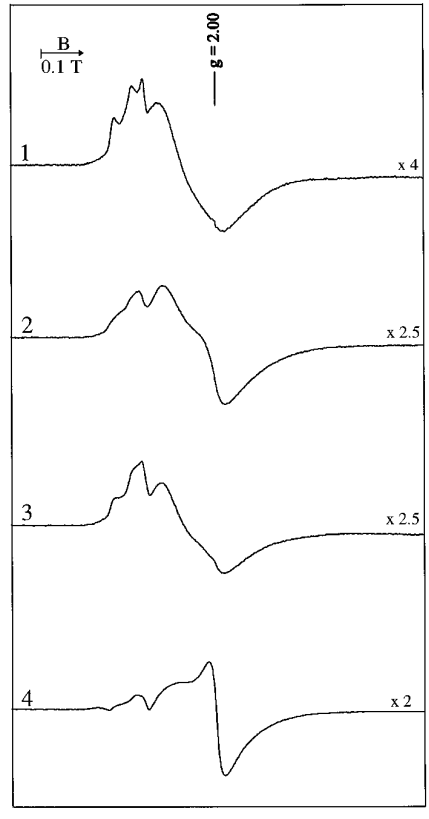

FIG. 8. EPR spectra of FeSC1 recorded at 300 K: The various treatments are the same as in Fig. 7.

cates that the ferric ions responsible for the signal are in mutual magnetic interaction. They should thus belong to small extraframework Fe–O clusters or to tiny ferric oxide particles exhibiting superparamagnetic or even ferromagnetic behavior which are formed in the zeolite channels upon calcination of the freshly prepared FeS material (28, 55) as also shown by the UV–vis and TPR results reported in the previous section. The fact that no signal is observed at g = 2 in the spectra of Figs. 7 and 8 (curves 1) indicates, again in agreement with previous findings in this paper, that in FeSC1 no ferric ions in perfect tetrahedral coordination are available after dehydration at 673 K. For such undistorted tetrahedral sites a $g_{eff} = 2.0$ is in fact expected, as observed for $FePO_4$ and for iron-containing zeolites such as the Fe–L and the Fe–sodalite recently reported by Goldfarb *et al.* (56).

The effect of a partial rehydration (the sample was put in contact with the vapour pressure of water for some 15 s) on the dehydrated sample is described by spectra 2 in Figs. 7 and 8 and is twofold. First, a new component arises at $g_{eff} = 2.0$ (signal *C*) that partially overlaps in the room temperature spectrum with the signal due to clustered ferric ions. Simultaneously the *A′* component tends to disappear while the *A* component is still present in the spectrum with high intensity but, due to the overlap between the various components, it is difficult to understand whether its intensity is actually affected by water adsorption. The features of the spectra of the thoroughly dehydrated sample (curves 1) are partially recovered by pumping off water at room temperature (curves 3 in the same figure) and fully recovered upon the vacuum treatment at 673 K.

The effect of ammonia admission on the dehydrated zeolite (60 Torr NH_3 at room temperature) is similar but more radical than that of water adsorption (spectra 4 in Figs. 7 and 8). The two spectra can be analyzed in terms of the presence of three components. The first one is the signal C at $g_{eff} = 2.0$ which is here larger than after water adsorption (spectra 2); the second one is the line *A* at $g_{eff} = 4.3$ which is now severely depressed again in comparison with the effect of water adsorption. A third component (signal *D*) arises at field values between those of *A* and *C* and overlaps with signal *B* (the signal due to clustered ferric ions), but is definitely different from this latter one. This can be seen by comparing the spectra recorded at 77 K and 298 K. The effect of the recording temperature (clearly visible in the spectra 1 and due to the non-Curie behavior of the extraframework clusters) is very different in spectra 4 where the modification caused by the higher intensity of line C at 298 K is no more appreciable. The two spectra 4 are practically identical (except for small variations in the relative intensities of the various components) to those observed after prolonged contact of the sample with water vapor (leading to a complete rehydration of the zeolite) and to those recorded for the ''as prepared'' FeS sample, still containing the undecomposed template. Furthermore, they are very close to those reported by Lin *et al.* (28) for a similar Fe-silicalite system also recorded on an ''as prepared'' hydrated sample. The signal labelled D seems to be the same as classified in Ref. 28 as signal III. The effect of ammonia coordination and of a substantial rehydration on the EPR spectra is therefore the same. The starting spectra of Figs. 7 and 8 are again attained upon thermovacuum treatment of the ammonia treated samples at 673 K.

The findings reported above are in general agreement with the description of the system that derives from the spectroscopic and TPR measurements reported in the previous paragraphs. In particular the following assignments can be proposed.

(1) Signals *A*, *A′*, and *A″* tend to transform into signal *C* upon admission into the zeolite of H_2O or NH_3. The g_{eff} of signal *C* (2.0) indicates that the corresponding Fe^{3+} species is highly symmetric (ZFS parameters are close to zero) and therefore corresponds to the isolated framework species reported in Scheme 4 where the presence of a positive ion (NH_4^+ or H_3O^+) or of water strongly hydrogen-bonded ensures the tetrahedral symmetry of the ferric sites. Evacuation of ammonia (or of water) leads to the distorted tetrahedral Fe^{3+} species characterized by the presence of the Si-Fe bridging hydroxyl reported in Scheme 5. The distortion of the tetrahedral crystal field introduces non-zero ZFS parameters which in turn cause the shift of the resonance lines from the region of $g = 2$ toward low magnetic field (line *A*, *A′*, and *A″*). On this point the data reported in the present paper differ from those of Lin *et al.* (28) due to the presence of the *A′* and *A″* components beside the main *A* one. The *A* component at $g_{eff} = 4.3$ is usually thought to be due to a strong rhombic distortion of the tetrahedral coordination of Fe^{3+} (that implies $D \neq 0$ and $E \neq 0$) while the *A′* one ($g_{eff} \cong 6$) should be assigned to a less distorted tetrahedron which maintains a C_{3v} axial symmetry (in such a case $D \neq 0$ and $E = 0$). A $g_{\perp} = 6$ is in fact expected for this kind of symmetry together with a $g_{\parallel} = 2.0$, usually not visible because of line broadening (28, 57). As to species *A″* we think that it should be related to a third type of distortion of the originally tetrahedral site, even though it cannot be totally excluded, on the basis of the present data, that *A″* could be a resolved component of the *A* signal related to some particular transition of the $S = 1/2$ system having $0 < E/D < 1/3$. In the light of these results the EPR technique suggests, more explicitly than the findings reported in the previous paragraphs, that the removal of the tetrahedral symmetry during the process of calcination and progressive dehydration of the zeolitic framework is a complex process leading to more than one type of distorted ferric site. The present results mainly show that all the families of centres corresponding to *A*, *A′*,

(and possibly *A″*) signals are variously distorted framework sites. Although on the basis of the reversible behaviour upon hydration–dehydration cycles it can be inferred that the majority of these low field signals corresponds to framework centres, it cannot be completely excluded that some of them or, alternatively, one of the three families corresponds to extraframework isolated sites undergoing a reversible process of solvation upon interaction with water or ammonia.

(2) The presence of the broad line (signal B) in Figs. 7 and 8 (spectra 1) whose intensity does not follow the trend predicted by the Curie law, indicates, as previously stated, that extraframework interacting ferric centres (likely to be small iron–oxygen clusters) have been generated by the calcination treatments performed to eliminate the template. The anomalous behavior with temperature in the corresponding spectra region is no longer observed when the sample is treated with ammonia. The interpretation that can be proposed to account for this effect involves two parallel phenomena.

The first one implies that ammonia adsorption on the small oxidic aggregates leads (at least for a fraction of the iron ions) to less interacting ferric moieties which should correspond to the *D* signal visible in Figs. 7 and 8 (spectra 4), which in fact is observable only when ammonia or water are contacted with the zeolite. Species *D*, however, is also reported in Ref. 28 where it is labelled as species III and assigned to framework ions having a coordination vacancy related to reactivity with incoming molecules. This assignment, however, cannot be confirmed on the basis of our data since, differently from what is shown in ref. 28, the trace of species *D* is completely absent in the thoroughly dehydrated material.

The second effect implies that the signal related to those (residual) magnetically interacting ferric ions still present in the ammonia treated material is buried in the lines due to *C* and *D* species which are rather intense. The problem is currently under investigation and we prefer, at this stage, to consider the *D* signal as the result of solvation effects on extraframework clustered ferric ions.

The above reported interpretation of the EPR data is schematically summarized in the following scheme (Scheme 6).

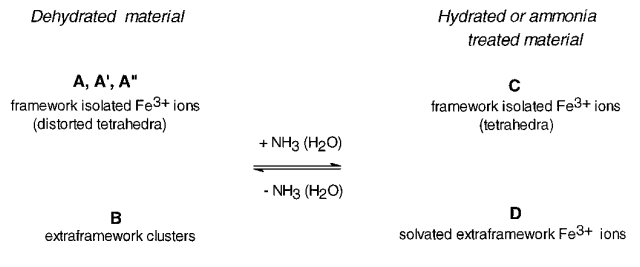

SCHEME 6

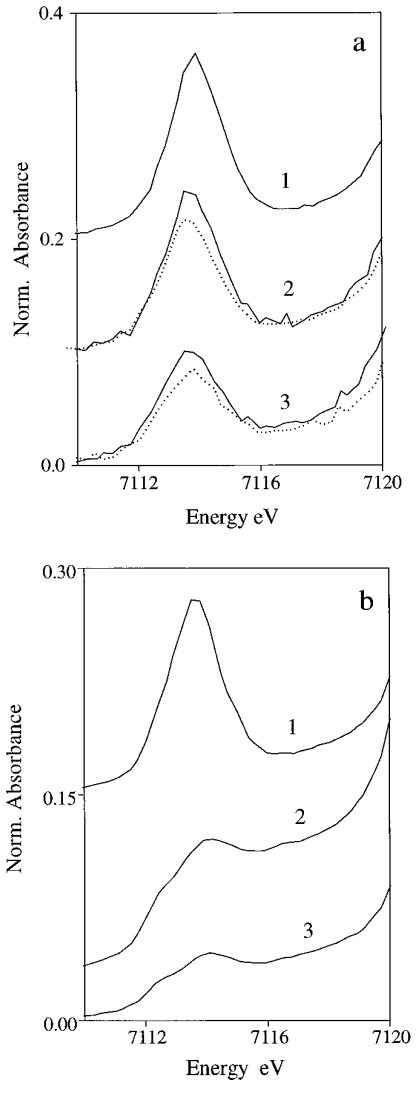

FIG. 9. X-ray absorption spectra. Pre-edge region: (a) Fe-silicalites: (1) FeS, (2) FeSC1 (full line in presence of 60 Torr of NH_3, broken line *in vacuo*); (3) FeSC2 (solid line in presence of 60 Torr of NH_3, broken line *in vacuo*); (b) reference compounds: (1) $FePO_4$; (2) Fe_2O_3; (3) FeOOH.

5. *XANES*

UV–visible and EPR data indicate that framework Fe^{3+} species are in a nearly perfect tetrahedral coordination in the presence of the template or of adsorbates like H_2O and NH_3 and that calcination treatment, at $T > 773$ K, induces the extraction of the Fe^{3+} from framework positions, with formation of oxidic microaggregates whose dimensions and reactivity towards adsorbates are not well known. As XANES spectroscopy is a powerful tool to investigate the local atomic coordination state, it has been utilized in this study to gain some additional information on the coordinative state of Fe^{3+} species and its changes upon interaction with adsorbates.

The K-edge adsorption spectra of Fe^{3+} exhibit a small pre-edge peak, or ''prepeak'', corresponding to transitions from 1s to 3*d*-like levels. In systems with octahedral symmetry these transitions are Laporte forbidden. Nevertheless, in real systems, where distortions from the perfect octahedral symmetry are very common, the loss of the inversion center and a partial mixing of *p* and *d* levels is often observed with subsequent gain in the intensity of the pre-edge transitions. On the contrary, systems with tetrahedral symmetry, and hence without an inversion center and with strong *d–p* mixing, are characterized by a strong peak in the pre-edge region due to the allowed transition from the ground state A_1 to the final state T_2 (33, 58–60).

The prepeak region of FeS, FeSC1, and FeSC2 (spectra 1, 2 and 3, respectively) is shown in Fig. 9a (spectra obtained in the presence of NH_3 are reported as full lines, while those obtained *in vacuo* are shown as dotted lines). In Fig. 9b the prepeak region of three model compounds with tetrahedral ($FePO_4$) and octahedral (Fe_2O_3 and γ-FeOOH) coordination are reported for the sake of comparison (spectra 1, 2 and 3, respectively).

The preedge spectra of Fe-silicalite samples are characterized by a well-defined single peak whose intensity, energy and full width at half maximum (FWHM) is sensitive to calcination treatments and to adsorbate interaction (33, 49). The complete list of data obtained for the samples in presence of ligands (template or NH_3) is reported in Table 1 together with those of $FePO_4$, while those of the samples *in vacuo* are listed in Table 2.

From Table 1 is it evident that on passing from sample FeS (spectrum 1) to FeSC1 (spectrum 2) and especially to FeSC2 (spectrum 3), the prepeak intensity decreases, and the FWHM increases.

The agreement of prepeak data obtained for FeS and FeSC1 samples with those of $FePO_4$ (which is considered a good model compound for tetrahedrally coordinated Fe^{3+} species) indicates that a high concentration of nearly perfect tetrahedrally coordinated Fe^{3+} species is present in these systems, in full agreement with the IR and UV–visible results.

TABLE 1

XANES Data of Fe-Silicalite Prepeak in Presence of Adsorbates

Sample	Intensity (%)	Peak position (eV)	FWHM (eV)
FeS	16.6	7113.9	2.1
FeSCl	15	7113.5	2.4
FeSC2	10	7113.5	2.7
$FePO_4$	13	7113.5	2.4

TABLE 2

XANES Data of Fe-Silicalite Prepeak *in Vacuo*

Sample	Intensity (%)	Peak position (eV)	FWHM (eV)
FeSC1	12	7113.9	2.4
FeSC2	8.5	7113.8	3.0

From the previous considerations, it is evident that the prepeak intensity is directly related to the percentage of Fe^{3+} in tetrahedral coordination (which substitute Si^{4+} in the framework). Consequently, the progressive intensity decrease induced by calcination (small in FeSC1 and large in FeSC2) accompanied by a clear broadening, indicates that the calcination procedure causes a progressive migration of framework Fe^{3+} species towards extraframework positions with formation of oxidic microaggregates. The persistence of a distinct (although broadened) single prepeak, without the splitting pattern characteristic of the model compounds with octahedral symmetry (60) (Fe_2O_3 and γ-FeOOH, curves 2 and 3 respectively in Fig. 9b) suggests that the fraction of large oxidic aggregates containing a high percentage of octahedral Fe^{3+} is still very low. The low concentration of bulky species is not surprising: in fact, if Fe_2O_3 clusters are formed inside the zeolite channels and at their intersection (diameter: 5.5 Å), only microaggregates with less than 3–5 Fe_2O_3 units can be formed, which contain a negligible proportion of bulky Fe^{3+} octahedral ions and a large fraction of low coordinated surface ions. NH_3 dosage on FeSC1 and FeSC2 induces a parallel intensity increase of the pre-peak: this suggests that the amount of Fe^{3+} ions interacting with adsorbates is analogous in FeSC1 and FeSC2. In conclusion:

(i) In FeSC1 most of the Fe^{3+} species are in the framework with a distorted tetrahedral symmetry (*in vacuo*) and tetrahedral symmetry (in presence of ligands).

(ii) FeSC1 contains also extraframework species in the form of oxidic clusters with very small dimensions where almost all Fe^{3+} species are exposed. These ions seem to reach a distorted tetrahedral symmetry in presence of ligands.

(iii) In FeSC2 nearly all the Fe^{3+} ions are in extraframework position and form aggregates containing a high concentration of surface ions which can interact with adsorbates assuming distorted tetrahedral symmetry. The evidence that in FeSC2 highly dispersed low-coordinated extraframework Fe^{3+} species are present is in perfect agreement with the high catalytic activity of this zeolite in oxidation reactions. This hypothesis, which could not be advanced on the basis of UV–visible data alone, represents a real novelty introduced by XANES data.

In the near edge region the spectra (reported in Fig. 10) are still consistent with the foregoing considerations.

A detailed interpretation of this spectroscopic region is not dealt with in this article: nevertheless, the evident similarity of FeS and $FePO_4$ spectra (curves 1, full and dotted lines, respectively) must be underlined. In fact both spectra are characterized by three maxima respectively at 7126.5, 7133.6, and 7146.7 eV in $FePO_4$ and at 7131.4, 7137.4, and 7148.2 eV in FeS. These features, considered as a fingerprint of tetrahedral structures (60), are less visible in FeSC1, also after NH_3 contact (curve 2, full line) and become scarcely present in FeSC2 treated in an analogous way (curve 3, full line). On the contrary, the spectra obtained *in vacuo* (curves 2 and 3, dotted lines) strongly depart from the expected tetrahedral profile showing the growth of a new maximum at 7130.6 eV.

6. *EXAFS*

The qualitative information deduced from XANES have been confirmed and completed with the quantitative data derived from EXAFS analysis. The main results can be summarized as follows.

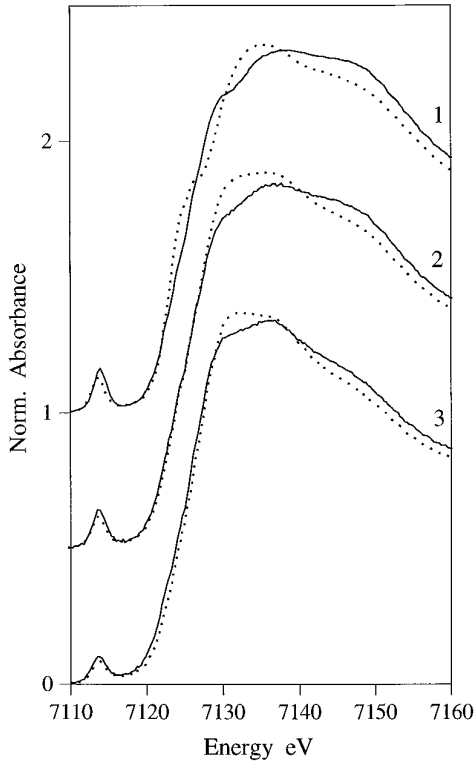

FIG. 10. X-ray absorption spectra. XANES region: (1) solid line FeS, dotted line $FePO_4$; (2) FeSC1 (full line in presence of NH_3, dotted line *in vacuo*); (3) FeSC2 (solid line in presence of 60 Torr of NH_3, dotted line *in vacuo*).

In all cases the χ(E) EXAFS signal, extracted from the adsorption spectra as described in the Experimental section, are characterized by the damped nature of the apparently single oscillation due to oxygen neighbours (49, 61). The Fourier transform of all the Fe-silicalite spectra and of $FePO_4$ show only one relevant maximum centred at 1.8–1.9 Å which is the value expected for the Fe-O distance in fourfold coordinated species (62). Nevertheless, the detailed EXAFS analysis is not straightfoward, for two main reasons:

(i) the intrinsically low intensity of the signal due to the low Fe content (1.71 wt%);

(ii) the relevant structural disorder due to the coexistence of many Fe^{3+} species with several coordination states (particularly in samples calcined at higher temperature).

While all the samples show very similar Fourier transform peak positions, on the contrary remarkable differences in the integrated area are observed. This is especially true for FeSC2 samples, both *in vacuo* and in the presence of NH_3. Consequently, before trying a quantitative analysis of the back-Fourier transform, it is better to discuss in more detail why FeSC2 is characterized by such weak Fourier transform peaks.

In comparison with FeS and FeSC1, whose peaks are very similar to those found for $FePO_4$ (model compound for tetrahedral Fe^{3+}) FeSC2 shows peaks characterized by a remarkable decrease of intensity. According to the usual relation connecting intensity and coordination number, this apparently suggests that Fe^{3+} can have coordination number lower than three. As structures with a Fe^{3+} coordination state so low are unknown and as we have no evidence of abundant presence of Fe^{3+} Lewis sites (49) upon CO and N_2 adsorption at low temperature (42, 43), this hypothesis is not convincing and an alternative hypothesis must be suggested.

To do this, let us assume that our system contains only a small fraction of homogeneous species (like residual framework Fe^{3+} species) giving a constructive contribution to the EXAFS signal, while the biggest fraction of species has a disordered coordination environment (like Fe^{3+} in nano-clusters $(Fe_2O_3)_n$ (with $2 < n < 5$) with Fe–O distances and coordination numbers spread over a large interval) and hence giving no spectral contribution at all. In such a situation the quantitative EXAFS analysis is not significant as the derived structural data give average coordination numbers and distances without any physical meaning.

For this reason a detailed spectral analysis and fits have been reported only for FeS and FeSC1 samples (*in vacuo* and in presence of NH_3).

The comparison between the back-Fourier transforms

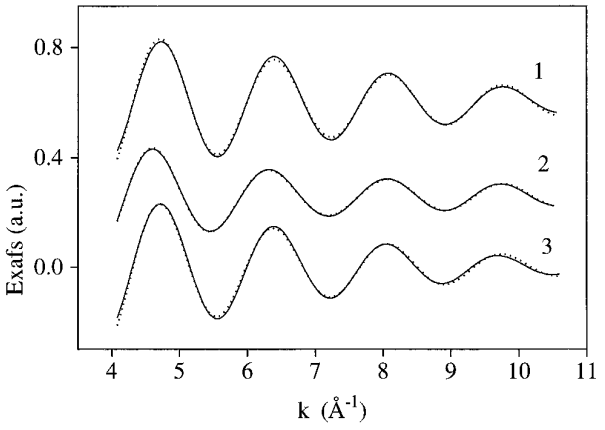

FIG. 11. EXAFS data: experimental results are given as the solid line, theoretical simulation as the dotted line: (1) FeS; (2) FeSC1 *in vacuo*; (3) FeSC1 in presence of 60 Torr of NH_3.

and the fits are shown in Fig. 11 while in Table 3 the derived structural data are reported.

The main results can be summarized as follows:

(i) FeS is characterized by the presence of Fe^{3+} 4-fold coordinated with a Fe–O distance of 1.85 Å. This distance is in perfect agreement with previous data for Fe^{3+} tetrahedrally coordinated (Fe-O in $FePO_4$ and in other compounds (62));

(ii) For FeSC1 *in vacuo* a two-oxygen shell fit is needed (three oxygens at 1.86 Å and 1 at 2.07 Å). The results are in agreement with simulations carried out using the standard lattice energy minimization reported in Refs. (63, 64), which suggest a distorted tetrahedral coordination for Fe^{3+} in Fe-silicalite due to the presence of the Fe-O(H) distance longer than the other three Fe–O (see Scheme 5);

(iii) The EXAFS spectrum of FeSC1 in the presence of NH_3 is fitted with a single oxygen-shell corresponding to Fe^{3+} surrounding more homogeneous than in FeSC1 *in vacuo*. In particular both coordination number and distances are compatible with tetrahedral Fe^{3+} species $[FeO_4]^-$ units hydrogen bonded to protonated ammonia (see Scheme 4). Unfortunately the presence of coordinated NH_4^+ cannot be confirmed by EXAFS data. A distinguishable contribution of extraframework species has not been quantitatively estimated; however, the lower intensity of the EXAFS oscillations observed in case of FeSC1 *in vacuo* (curve 2) may include also the effects of extraframework species.

TABLE 3

Fitting Results for the EXAFS Spectra of FeS and FeSC1 Samples

Sample	$N \pm 0.03$	R (Å) $\pm$ 0.007	$\sigma^2\ 10^{-3}$ (Å^2)	Fit
FeS	4.09	1.851	0.18	4.57×10^{-3}
FeSC1 *in vacuo*	2.85	1.865	0.21	1.17×10^{-3}
(two shell fit)	1.07	2.100	0.21	
FeSC1 + NH_3	4.07	1.857	0.35	4.65×10^{-3}

CONCLUSION

The coordinate state of Fe^{3+} in Fe-silicalite has been investigated by IR, Raman, UV–visible, EPR, XANES, and EXAFS spectroscopies and TPR. The simultaneous application of several physical techniques has enabled the following of the evolution of the Fe^{3+} environment after thermal treatments and interaction with adsorbates. As prepared Fe-silicalite is characterized by isolated Fe^{3+} located in the framework in substitutional position. In the presence of the template, Fe^{3+} is in tetrahedral symmetry, as inferred from UV–visible reflectance and XANES data and confirmed by EXAFS results. Template burning (with the associated water production) causes the partial breaking of some bonds connecting iron with the oxygen of the framework and induces the formation of oxidic aggregates. At 773 K this phenomenon is only partial, as only 20–25% of the Fe^{3+} is involved, but at 973 K almost all Fe^{3+} species are concerned, as documented by TPR data and by spectroscopic measurements. In particular, by increasing the calcination temperature (in the 773–973 K range) we observe: (i) the erosion of the IR band due to Brønsted sites; (ii) the erosion of the IR and Raman framework stretching modes concerning $[FeO_4]^-$ units; (iii) the progressive decrement of the pre-edge XANES peak and (iv) the disappearance of the UV–visible features characteristic of isolated Fe^{3+} species and the appearance of bands characteristic of clustered $(Fe_2O_3)_n$ species. Finally, under high vacuum conditions Fe^{3+} species show reduced symmetry as documented by the broad nature of the UV–visible, EPR, and XANES spectra; on the contrary in the presence of ligands such as H_2O and NH_3, Fe^{3+} centres are characterized by less distorted symmetries. In particular, on the sample calcined at 773 K, a tetrahedral symmetry is inferred.

ACKNOWLEDGMENTS

Support from CNR (Progetto Strategico Chimica Fine II) and from MURST (40%) is gratefully acknowledged. We thank the authors of Ref. (63) for communicating the results of their simulations prior to publication. We are also indebted to F. Boscherini for fruitful discussions and to F. Villain for providing helpful assistance during the EXAFS measurements at LURE.

REFERENCES

1. Flanigen, E. M., Bennett, J. M., Grose, R. W., Cohen, J. P., Patton, R. L., Kirchner, R. M., and Smith, J. V., *Nature* **271,** 512 (1978).

2. Szostak, R., and Thomas, T. L., *J. Catal.* **100,** 555 (1986).
3. Szostak, R., Nair, V., and Thomas, T. L., *J. Chem. Soc. Faraday Trans 1* **83,** 487 (1987).
4. Calis, G., Frenken, P., de Boer, E., Swolfs, A., and Hefni, M. A., *Zeolites* **7,** 319 (1987).
5. Borade, R. B., *Zeolites* **7,** 399 (1987).
6. Ratnasamy, P., and Kumar, R., *Catal. Today* **9,** 341 (1991).
7. Vorbeck, G., Richter, M., Fricke, R., Parlitz, B., Screier, E., Szulmewsky, K., and Zibrowius, B., *in* "Catalysis and Adsorption by Zeolites" (G. Öhlmann, H. Pfeifer and R. Fricke, Eds.), Stud. Surf. Sci. Catal. Vol. 65, p. 631, Elsevier, Amsterdam, 1991, and references therein.
8. Maegher, A., Nair, V., and Szostak, R., *Zeolites* **8,** 3 (1988).
9. Brückner, A., Lück, R., Wieker, W., Fahlke, B., and Mehner, H., *Zeolites* **12,** 380 (1992).
10. Ulan, J. G., Gronsky, R., and Szostak, R., *Zeolites* **11,** 466 (1991); **11,** 472 (1991).
11. Szostak, R., *in* "Introduction to Zeolite Science and Practice," (H. van Bekkum, E. M. Flanigen and J. C. Jansen, Eds.), Stud. Surf. Sci. Catal., Vol. 58, p. 153. Elsevier, Amsterdam, 1991, and references therein.
12. Kharitonov, A. S., Sheveleva, G. A., Panov, G. I., Sobolev, V. I., Pauskhtis, Y. A., and Romannikov, V. N., *Appl. Catal. A* **98,** 33 (1993).
13. Panov, G. I., Sheveleva, G. A., Kharitonov, A. S., Romannikov, V. N., and Vostrikova, L. A., *Appl. Catal. A* **82,** 31 (1992).
14. Kan, Q., Wu, Z., Xu, R., and Liu, X., *J. Mol. Catal.* **74,** 223 (1992).
15. Ratnasamy, P., Borade, R. B., Sivasankar, S., and Hedge, S. G., *Acta Phys. Chem.* **31,** 137 (1985).
16. Ho Kim, J., Namba, S., and Yashima, T., *Appl. Catal. A* **83,** 51 (1992).
17. Sobolev, V. I., Panov, G. I., Kharitonov, A. S., Rommanikov, V. N., Volodin, A. M., and Ione, K. G., *J. Catal.* **139,** 435 (1993).
18. Panov, G. I., Sobolev, V. I., and Kharitonov, A. S. "Catalytic Science and Technology," p. 171. 1991.
19. Sobolev, V. I., Panov, G. I., Kharitonov, A. S., Romannikov, V. N., and Volodin, A. M. *Kinet Katal.* **34,** 797 (1993).
20. Panov, G. I., Sobolev, V. I., and Kharitonov, A. S., *J. Mol. Catal.* **61,** 85 (1990).
21. Kikuchi, E., Yogo, K., Tanaka, S., and Abe, M. *Chem. Lett.* 1063 (1991).
22. Yogo, K., Tanaka, S., Ono, T., Mikami, T., and Kikuchi, E., *Micropor. Mater.* **3,** 39 (1994).
23. Inui, T., Iwamoto, S., Kojo, S., and Yoshida, T., *Catal. Lett.* **13,** 87 (1992).
24. Inui, T., Matsuda, H., Yamase, O., Nagata, H., Fukuda, K., Ukawa, T., and Miyamoto, A., *J. Catal.* **98,** 491 (1986).
25. Handreck, G. P., and Smith, T. D., *J. Chem. Soc. Faraday Trans 1* **85,** 3195 (1990).
26. Martin, A., Nowak, S., Luche, B., Wieker, W., and Fahlke, B., *Appl. Catal.* **57,** 203 (1990).
27. Kim, G. J., and Ahn, W. S., *Appl. Catal.* **71,** 55 (1991).
28. Lin, D. H., Coudurier, G., and Vedrine, J. C., *in* "Zeolite: Facts, Figures, Future" (P. A. Jacobs and R. A. van Santen, Eds.), Stud. Surf. Sci. Catal., Vol. 49, p. 1431 Elsevier, Amsterdam, 1989.
29. Nair, V., Szostak, R., Agrawal, P. K., and Thomas, T. L., *in* "Catalysis 1987" (J. W. Ward, Ed.), Stud. Surf. Sci. Catal. Vol. 38, p. 209 Elsevier, Amsterdam, 1988.
30. Parrillo, D. J., Lee, C., Gorte, R. J., White, D., and Farneth, W. E., *J. Phys. Chem.* **99,** 8745 (1995).
31. Chu, C. T-W., and Chang, C. D. *J. Phys. Chem.* **89,** 1569 (1985).
32. Datka, J., and Abranowicz, T., *J. Chem. Soc. Faraday. Trans.* **90,** 2417 (1994).
33. Bordiga, S., Geobaldo, F., Lamberti, C., Zecchina, A., Boscherini, F., Genoni, F., Leofanti, G., Petrini, G., and Padovan, M., *Nucl. Instr. Meth. B* **97,** 23 (1995).
34. Zecchina, A., Bordiga, S., Spoto, G., Marchese, L., Petrini, G., Leofanti, G., and Padovan, M., *J. Phys. Chem.* **96,** 4985 (1992).
35. Michalowicz, A., Ph.D. thesis, Université Paris Vol de Marne, 1990.
36. James, F., and Roos, M., *Comput. Phys. Commun.* **10,** 343 (1975).
37. McKale, A. G., Veal, B. W., Paulikas, P. A., Chan, S. K., and Knapp, G., *J. Am. Chem. Soc.* **110,** 3763 (1988).
38. Zecchina, A., Bordiga, S., Spoto, G., Marchese, L., Petrini, G., Leofanti, G., and Padovan, *J. Phys. Chem.* **96,** 4991 (1992).
39. Zecchina, A., Bordiga, S., Spoto, G., Scarano, D., Petrini, G., Leofanti, G., Padovan, M., Otero Areán, C., *J. Chem. Soc. Faraday Trans.* **88,** 2959 (1992).
40. Scarano, D., Zecchina, A., Bordiga, S., Geobaldo, F., Spoto, G., Petrini, G., Leofanti, G., Padovan, M., and Tozzola, G., *J. Chem. Soc. Faraday Trans.* **89,** 4123 (1993).
41. Pimentel, G. C., and McClellan, A. L., "The Hydrogen Bond," Chap. 3. Freeman, San Francisco, 1960.
42. Bordiga, S., Lamberti, C., Geobaldo, F., and Zecchina, A. Manuscript in preparation.
43. Kustov, L. M., Kazansky, V. B., and Ratnasamy, P., *Zeolites* **7,** 79 (1987).
44. Gonzalez-Vilchez, F., and Griffith, W. P., *J. Chem. Soc. Dalton* 1416 (1972).
45. Gonzalez-Vilchez, F., and Griffith, W. P., *An. Quim.* **69,** 617 (1973).
46. Figgis, B. N., "Introduction to Ligand Fields," Wiley, New York, 1966.
47. Inui, T., Nagata, H., Takeguchi, T., Iwamoto, S., Matsuda, H., and Inoue, M., *J. Catal.* **139,** 482 (1993).
48. Lehmann, G., *Z. Phys. Chem. Neue Folge* **72,** 279 (1970).
49. Patarin, J., Tuilier, M. H., Durr, J., and Kessler, H., *Zeolites* **12,** 70 (1992).
50. Tippins, H. H., *Phys. Rev. B* **1,** 126 (1970).
51. Bongiovanni, R., Pellizzetti, E., Borgarello, E., and Meisel, D., *Chim. l'Indust.* **4,** 261 (1994).
52. Jentys, A., Warecka, G., Derewinski, M., and Lercher, J. A., *J. Phys. Chem.* **93,** 4837 (1989).
53. Pelmenschikov, A. G., and van Santen, R. A., *J. Phys. Chem.* **97,** 10678 (1993).
54. Hurst, N. W., Gentry, S. J., Jones, A., and McNicol, B. D., *Catal. Rev. Sci. Eng.* **24,** 233 (1982).
55. Iton, L. E., Beal, R. B., and Hodul, D. T., *J. Mol. Catal.* **21,** 151 (1983).
56. Goldfarb, D., Bernardo, M., Strohmaier, K. G., Vaughan, D. E. W., and Thomann, H. *J. Am. Chem. Soc.* **116,** 6344 (1994).
57. Castner, T., Newell, G. S., Holton, W. C., and Slichter, C. P., *J. Chem. Phys.* **32,** 668 (1960).
58. Bordiga, S., Coluccia, S., Lamberti, C., Marchese, L., Zecchina, A., Boscherini, F., Buffa, F., Geononi, F., Leofanti, G., Petrini, G., and Vlaic, G., *J. Phys. Chem.* **98,** 4125 (1994); *Catal. Lett.* **26,** 195 (1994).
59. Combes, J. M., Manceau, A., Calas, G., and Bottero, J. Y., *Geochim. Cosmochim. Acta* **53,** 583 (1989).
60. Calas, G., and Petiau, J., *Solid State Commun.* **48,** 625 (1983).
61. Axon, S. A., Fox, K. K., Carr, S. W., and Klinowski, J., *Chem. Phys. Lett.* **189,** 1 (1992).
62. Geiger, C. A., Henry, D. L., Bailey, S. W., and May, J. J., *Clays Clay Miner.* **31,** 97 (1983).
63. Lewis, D. W., Sankar, G., Catlow, C. R. A., Carr, S. W., and Thomas, J. M., *Nucl. Instr. Meth. B* **97,** 44 (1995).
64. Lewis, D. W., Sankar, G., Catlow, C. R. A., and Carr, S. W., *J. Phys. Chem.* **99,** 2377 (1995).